

## Validation of a 3D bistatic microwave scattering measurement setup

Christelle Eyraud,<sup>1,2</sup> Jean-Michel Geffrin,<sup>1</sup> Pierre Sabouroux,<sup>1</sup>  
Patrick C. Chaumet,<sup>1</sup> Hervé Tortel,<sup>1</sup> Hugues Giovannini,<sup>1</sup> and Amélie Litman<sup>1</sup>

Received 29 January 2008; revised 28 April 2008; accepted 8 May 2008; published 28 August 2008.

[1] We present a 3D spherical bistatic experimental setup developed in the anechoic chamber of Institut Fresnel in Marseille, France, for scattering measurements of targets in the microwave domain, both in copolarization and cross-polarization. We first describe the geometry of the setup, the measurement protocol, and the calibration process. The results obtained for different metallic and dielectric targets are then compared to numerical simulations, computed either using the coupled dipole method or Mie theory. These comparisons are used to validate the algorithms and the setup, as well as to provide information on the accuracy of the measurements.

**Citation:** Eyraud, C., J.-M. Geffrin, P. Sabouroux, P. C. Chaumet, H. Tortel, H. Giovannini, and A. Litman (2008), Validation of a 3D bistatic microwave scattering measurement setup, *Radio Sci.*, 43, RS4018, doi:10.1029/2008RS003836.

### 1. Introduction

[2] Considerable effort have been undertaken for measuring scattered fields in monostatic and multistatic configurations in the microwave domain. In this context, it has been proposed laboratory-controlled experiments to constitute databases which are useful for the scientists working on the theoretical aspects of scattering. To our knowledge, there is a rather limited number of publications devoted to the presentation of scattering measurements for three-dimensional objects in which both magnitude and phase are presented [Fortuny-Guasch, 2002; Gustafsson, 1996; Gurel *et al.*, 2003; Kahny *et al.*, 1992; Coté, 1992], and even fewer when the receiving antennas are outside of the plane containing the source and the target [Hauck *et al.*, 1998]. This is the goal of the present paper.

[3] Performing laboratory controlled measurements presents several advantages, as highlighted by Coté [1992]. Indeed, comparing measured and simulated fields permits one to validate both the measurement protocol and the simulation algorithms. In particular, such comparisons are good means for debugging simulation codes which are tedious to implement (e.g., three-

dimensional configurations) and/or computationally intensive. Moreover, such comparisons can help to define the range of validity of the algorithms. Indeed, numerical methods are seldom exact, except if the obstacles have canonical shapes. For reasons of speed, complexity or limitations of memory, 3D scattering forward solvers are typically based on approximations, which take into account all available information on the nature of the scatterers (positions, shapes, ...). In this work, we present comparisons between measured scattered fields and simulated ones thanks to two computer codes. The first code is based on Mie theory. The second code uses the coupled dipole method (CDM). For these comparisons, the characteristics (shape, permittivity) of the objects are assumed to be perfectly known and the algorithms are employed within their domain of validity. Moreover, for the chosen frequency range, the size of the targets compared to the wavelength is such that the number of discretization points needed for the convergence of the numerical algorithms is compatible with the use of a personal computer.

[4] This study can also be considered as a prerequisite step toward super-resolution inverse 3D scattering applications [Borden, 2002], where people are interested in determining the dielectric characteristics of unknown scatterers via their electromagnetic signatures. Indeed, we will show that with our measurement setup, using classical free space measurement and by taking into account scattering phenomena, we are able to determine the permittivity of our dielectric target at approximately 1% accuracy by minimizing the differences between the simulated and measured scattered fields.

<sup>1</sup>Institut Fresnel, Aix-Marseille Université, CNRS, Ecole Centrale Marseille, Domaine Universitaire de Saint-Jérôme, Marseille Cedex, France.

<sup>2</sup>Now at Laboratoire de Planétologie de Grenoble, Grenoble Cedex, France.

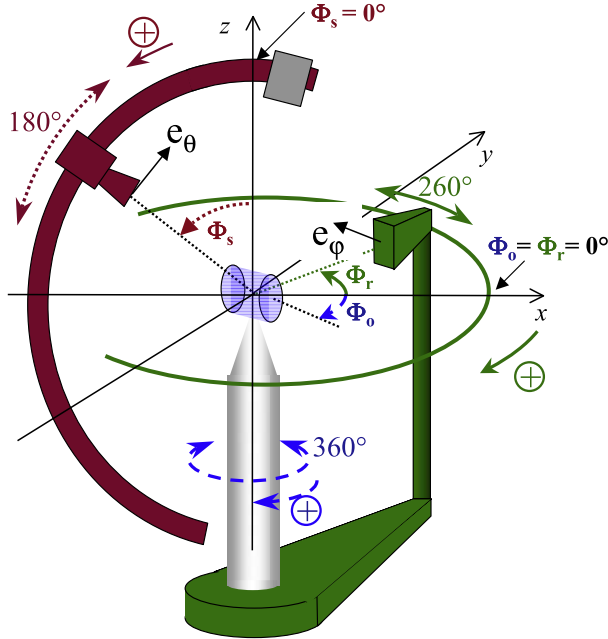


**Figure 1.** Schematic representing the excursion of the different motors. The target (represented here by a cylinder) is placed at the center of the setup on a polystyrene arm. It can rotate on itself  $360^\circ$ , with a position angle described by  $\phi_o$ , to create multi-incidences. The receiving antenna, whose position is defined by  $\phi_r$ , is positioned in the azimuthal plane and, because of the mechanical limitations of the arch, its excursion is not complete ( $-130^\circ < \phi_r < 130^\circ$ ). The transmitting antenna can move along the arch. Its position is defined by  $\phi_s$  ( $-11^\circ < \phi_s < 169^\circ$ ).

[5] As one of the final application of these measurements is 3D inverse scattering, our objective is to measure the scattered fields all around the target and even in the transmission region with a minimum of angular exclusions. The best would be to fill in the entire Ewald sphere with multiple incidence-receiving directions as well as multiple frequency information. Thus we have chosen to reject any time domain technique to extract the target contribution in the measured fields. The drawbacks of such a choice are mainly appearing when the scattered fields are becoming small compared to the measured fields, leading to a certain sensitivity to the dynamic of the setup and to drift phenomena. Indeed, the scattered field is not measured directly but obtained from the subtraction of two measured fields.

[6] Comparing experimental and simulated fields allows us to quantify the accuracy and the performance of the apparatus [Eyraud, 2006]. Let us remark that for all the measurements presented therein, we have chosen to use a very simplified calibration process in order to

highlight the intrinsic characteristics of our setup. In this context, a single calibration coefficient is defined [*van den Berg et al.*, 1995], which has been adapted to take into account drift errors.

[7] The present paper provides a series of experimental results of fields scattered by 3D metallic and dielectric targets. These experiments have been carried out in the anechoic chamber of the Centre Commun de Ressources Micro-Ondes (CCRM), managed, for this topic, by the researchers of Institut Fresnel, in Marseille, France. These measurements were obtained for antennas positioned on a 4 m diameter sphere surrounding the targets and for all the polarization cases. Although the setup was designed for measurements in the frequency range [1–26] GHz, we only present here the results obtained in the frequency range [2–18] GHz because of restrictions inferred by the mixers and the antennas range. The amplitude and, more specifically, the phase of the scattered fields have been measured.

[8] This paper is divided into 7 sections. Section 2 provides a description of the experimental setup and of the measurement protocol. The calibration process is then described in section 3. Section 4 provides a short presentation of the modeling codes. Section 5 presents the comparisons between simulated and measured fields obtained for four different targets. Finally, section 6 illustrates the accuracy of our measurement system. Some concluding remarks are presented in section 7.

## 2. Experimental Setup

### 2.1. Geometrical Arrangement

[9] All the experiments have been made in the Faraday anechoic chamber (14.5 m  $\times$  6.5 m  $\times$  6.5 m) of CCRM already described in previous papers [Sabouroux et al., 2005; Geffrin et al., 2005]. A schematic of the setup is presented in Figure 1. Its main specificity consists of a semi-circular vertical arch along which two wagons are able to move, enabling measurements outside of the azimuthal plane. The antennas fixed on these wagons can be used either as transmitter or receiver thanks to a switching device. Therefore the incident direction is not necessarily in the plane described by the receiving directions. It is worth noticing that there are few scattered field measurements which have been realized with such a configuration. In the study of Hauck et al. [1998], results have been presented but for a single frequency.

[10] The object under study is placed on a support at the center of the 4 m diameter measurement sphere. The support consists in an expanded polystyrene cylinder which is assumed to be transparent. The cylinder, and therefore the target, can rotate around the vertical z-axis, with an angle  $\phi_o$  varying from  $0^\circ$  to  $360^\circ$  (Figure 1). The transmitting antenna is displaced along the arch in order

**Table 1.** Description of the Dimensions and Characteristics of the Four Scatterers<sup>a</sup>

Material Shape	Inox Sphere	Altuglass Sphere	Ertalon Cylinder	Polyethylene Cube
Diameter, mm	70.00	50.75	80.00	×
Height, mm	×	×	80.00	79.90
EpsiMu $\epsilon_r$ , 5%	×	2.50	3.00	2.30
Optimized $\epsilon_r$ , 1%	×	2.60	3.05	2.35
National Institute of Standards and Technology $\epsilon_r$ , $\pm 0.03$	×	2.61	3.00	2.39

<sup>a</sup>The NIST permittivities values are taken from *Riddle et al.* [2003].

to change the angle of incidence  $\phi_s$  from  $-11^\circ$  to  $169^\circ$ . This limitation is due to the dimensions of the arch. Thus, when the transmitting antenna is in the azimuthal plane (respectively above the target), the angle of incidence corresponds to  $\phi_s = 90^\circ$  (respectively  $\phi_s = 0^\circ$ ). The receiving antenna is positioned on an arm that can rotate around the vertical  $z$ -axis in the  $xOy$  plane. The presence of the arch foot limits the excursion of the receivers so that the receiving angle  $\phi_r$  is restricted between  $-130^\circ$  and  $130^\circ$ . The distance between the source and the object (respectively between the receiver and the object) has been measured to be  $1796 \pm 2$  mm (respectively  $1795 \pm 2$  mm). As our goal is to measure the scattered fields of 3D targets, we have chosen to perform our measurements as radiation patterns corresponding to the radiation of the secondary currents induced inside the scatterer. Thus, to be able to fill the sphere of measurements using reciprocity, it was easier to keep the same radius for the emitters and the receivers. The two antennas can also be rotated on their support in order to change the direction of polarization. Thus, with this setup, measurements of the  $e_\theta$  and the  $e_\phi$  components of the electromagnetic field can be performed.

## 2.2. Measurement Apparatus

[11] The measuring equipment is based on a Vector Network Analyser (VNA) (Agilent HP 8510) used in a multi-source configuration with two synthesizers and two external mixers [Agilent 85301B/C Antenna Measurement Systems]. Usually, the mixers are positioned as close as possible to the antennas. These mixers perform frequency translation, from high to low frequency (here 20 MHz) to reduce the propagation length of the high-frequency waves in the cables. Indeed, as it is well known, the propagation at high frequencies in coaxial cables suffers from attenuation as well as from strong sensitivity to any movement, cable bent or even to (room) temperature variations. In our setup, the source mixer is nevertheless kept far from the source antenna (9 m of coaxial cable). To limit the number of running cables around the arch, and to get the highest source excursion using our two wagons in conjunction with the switch, we have made the technical choice of keeping these 9 m of high-frequency cables. Thus the compar-

isons presented in this paper are also here to show that this choice was pertinent.

[12] The transmitting and receiving antennas are wide frequency range linearly polarized ridged horn antennas (ARA DRG118). The polarization has been chosen such that the emitting antenna is always along  $e_\theta$  and the receiving antenna is rotated to measure either the  $e_\theta$  or  $e_\phi$  field component.

## 2.3. Measurement Protocol

[13] The measurement protocol has been carefully selected to reduce as much as possible systematic measurement errors as well as the acquisition time. In particular, previous work [Eyraud, 2006] has shown that if the field measured with the target (the total field) and the field measured without it (the incident field) are not acquired with a receiving antenna moving in the same direction of rotation, the difference between these two fields (the scattered field) presents important oscillations, which are due to some mechanical looseness. Therefore the receiving antenna is moved clockwise and counter clockwise.

[14] The measured field amplitudes and phases are functions of the receiving antenna position  $\phi_r$ , the emitting antenna angular position  $\phi_s$ , and the target orientation  $\phi_o$ , for both  $e_\theta$  and  $e_\phi$  field components. The total field measurement is performed in the following way:

For Polar =  $\theta\phi$  and  $\theta\theta$  (plus  $\phi\theta$  and  $\phi\phi$  if needed),  
 For  $\phi_s = -11^\circ$  to  $169^\circ$  {Move emitter},  
 For  $\phi_o = -0^\circ$  to  $360^\circ$  {Rotate the target},  
 For  $\phi_r = -130^\circ$  to  $130^\circ$  and back to  $-130^\circ$   
 {Move receiver clockwise and counter-clockwise},  
 Stop, Wait  
 For  $f = 2$  to  $18$  GHz {Change frequency}.  
 Measure field amplitude and phase

[16] The delay after the stop in the mechanical movement (200 ms here) is needed to stabilize all potential unsteady parts (antennas, cables, . . .) as they may interfere with the measurement and have some noise effects. We also apply a slow deceleration rate before stopping the antenna to limit these oscillations. To reduce measurement

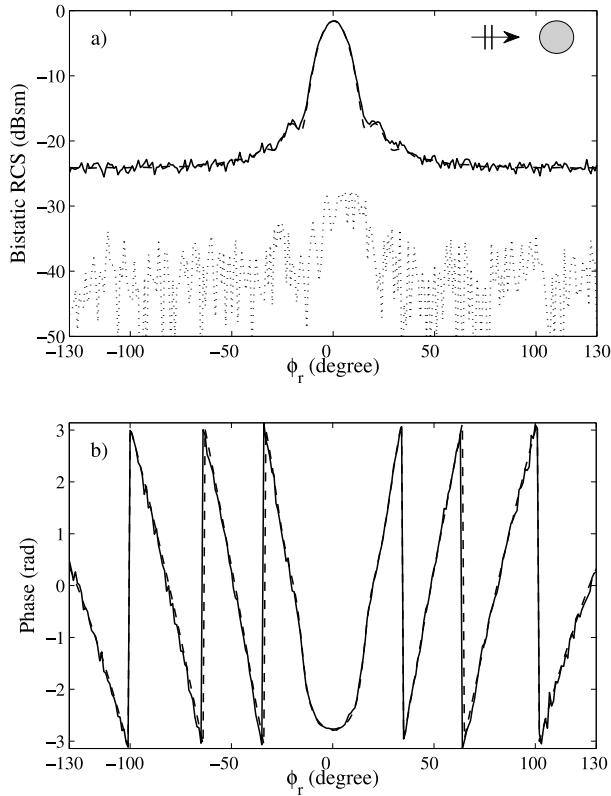


**Figure 2.** Comparison of (a)  $|E_{d,\theta\theta}|$  and (b)  $\arg(E_{d,\theta\theta})$ , measured (full line) and simulated (dashed line).  $|E_{d,\theta\varphi}|$  is also plotted in dotted line in Figure 2a to show the magnitude difference. This result is obtained for the metallic sphere at 18 GHz and for  $\phi_s = 90^\circ$  ( $\mathcal{F}_{\theta\theta} = 0.004$ ).

errors such as cables disconnection, the target is then removed and the incident field is measured with the same protocol, except for the target's rotation. The scattered field is finally obtained by subtracting the incident field to the total field. To obtain exploitable scattered fields, the incident field must present a phase accuracy of tenth of radians for all receiver locations. As it is difficult to guaranty such level of accuracy with computed incident fields, the incident field is also measured.

[17] The necessity to extract the relevant information from two different measurements makes good stability and a sufficient dynamic really essential. For example, in certain cases, the measurements of the fields in the forward direction (in front of the sources) must be made with a very high accuracy. This is the case for weak scatterers (scatterers smaller than the wavelength or scatterers with a small permittivity contrast), where the amplitude of the scattered field can be very low compared to the amplitude of the measured fields (in our dielectric sphere case, this difference can reach up to 25 dB).

[18] This two-steps procedure introduces fluctuations coming from mechanical looseness or drifts, leading to strong errors. These errors even increase when the scattered field is small compared to the incident one. Notably, we are obliged to correct for the drift (around hundredth of radians in phase and tenth of percent in magnitude) which can occurs between the total field measurement and the incident field measurement [Eyraud et al., 2006; Eyraud, 2006]. Thanks to this efficient drift correction, the measurements are now fully exploitable.

### 3. Calibration Protocol

[19] Different calibration processes have been proposed for multistatic experimental systems, enabling full polarization corrections. In particular, Kahny et al. [1992], Whitt et al. [1991], and Bradley et al. [2005] propose techniques which allow to correct for all distortions due to transmitting and receiving antennas. Here, in order to show the intrinsic performances of our system, we have

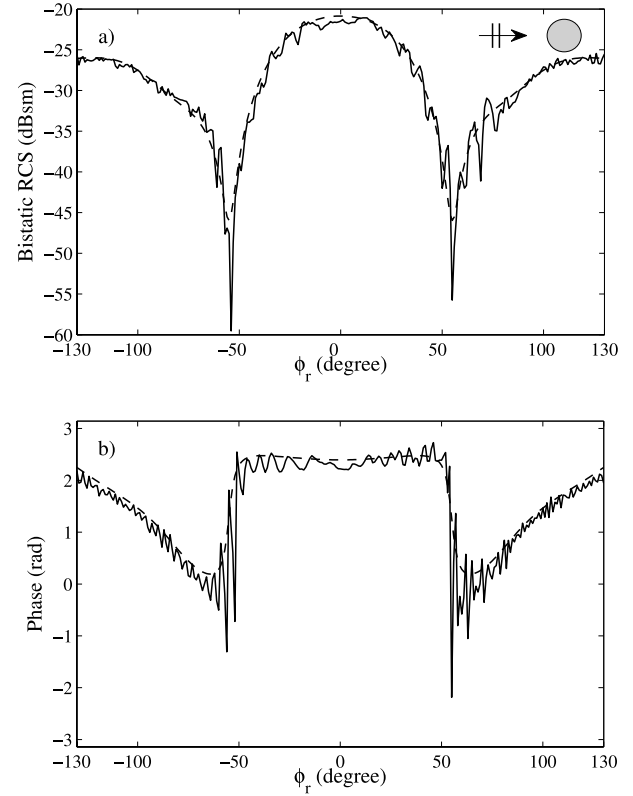


**Figure 3.** Comparison of (a)  $|E_{d,\theta\theta}|$  and (b)  $\arg(E_{d,\theta\theta})$ , measured (full line) and simulated (dashed line). This result is obtained for the metallic sphere at 8 GHz and for  $\phi_s = 30^\circ$  ( $\mathcal{F}_{\theta\theta} = 0.029$ ).

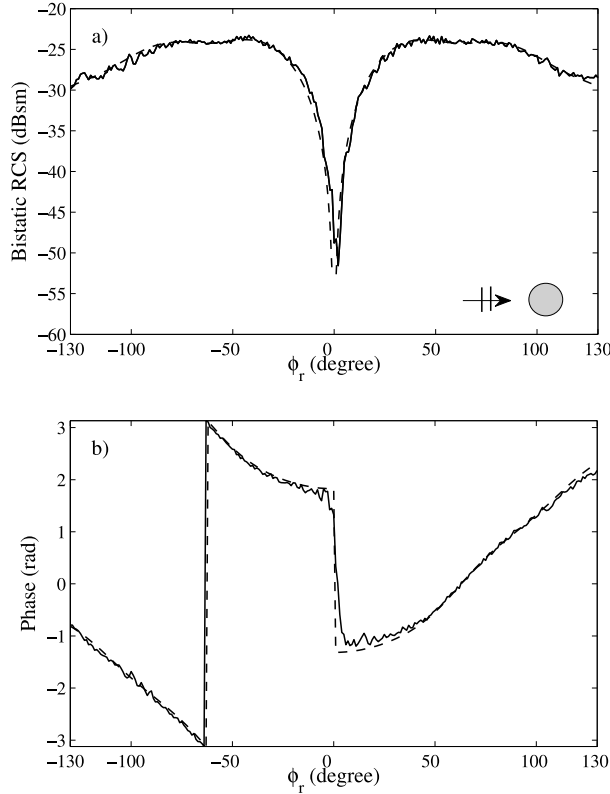


**Figure 4.** Same configuration as in Figure 3 but for  $|E_{d,\theta\varphi}|$  and  $\arg(E_{d,\theta\varphi})$  ( $\mathcal{F}_{\theta\varphi} = 0.007$ ).

decided to provide a very fast and simple calibration protocol, based on a single complex coefficient.

[20] With our ridged horn antenna, the isolation between the co-polarization and the cross-polarization for a non-depolarizing target (a stainless sphere) is larger than 20 dB over the 2–18 GHz frequency band. For this reason, we have decided to neglect the spurious polarization term during calibration according to Hauck *et al.* [1998] and Sarabandi *et al.* [1990]. Moreover, we assume that the antennas distortions do not depend on the polarization state. Finally, we assume that the only difference between the experimental and the simulated scattered fields relies in a complex coefficient  $D$ , obtained through the comparison of the unique  $\theta\theta$  polarization.  $D$  is assumed to be constant for all receiver directions, all source positions and all target orientations. The reference target is chosen as a stainless sphere ( $\phi = 70$  mm), which is considered to be perfectly conducting.

[21] In order to take into account the drift difference existing between the scattered field of the reference target used for calibration and the scattered field of the studied target,  $D$  is defined as the product of a standard calibration term [van den Berg *et al.*, 1995] and of a drift

correction term [Eyraud, 2006] which compares the two incident fields, such as

$$D = \frac{\sum_{\phi_o} \sum_{\phi_r} E_{d,\theta\theta}^{simu,ref} \overline{E_{d,\theta\theta}^{meas,ref}}}{\sum_{\phi_o} \sum_{\phi_r} |E_{d,\theta\theta}^{meas,ref}|^2} \times \frac{\sum_{\phi_r} E_{i,\theta\theta}^{meas,ref} \overline{E_{i,\theta\theta}^{meas}}}{\sum_{\phi_r} |E_{i,\theta\theta}^{meas}|^2} \quad (1)$$

where  $E_{d,\theta\theta}^{simu,ref}$  (respectively  $E_{d,\theta\theta}^{meas,ref}$ ) denotes the  $e_\theta$  component of the simulated (respectively measured) scattered field for the reference target, (the first  $\theta$  subscript being related to the polarization of the emitting antenna).  $E_{i,\theta\theta}^{meas}$  (respectively  $E_{i,\theta\theta}^{meas,ref}$ ) corresponds to the  $e_\theta$  component of the incident field measured for the studied (respectively reference) target.

[22] This minimal calibration is then applied to measurements out of the azimuthal plane. The comparisons between measured and simulated fields presented in the next section show that this calibration is sufficient for various targets, for

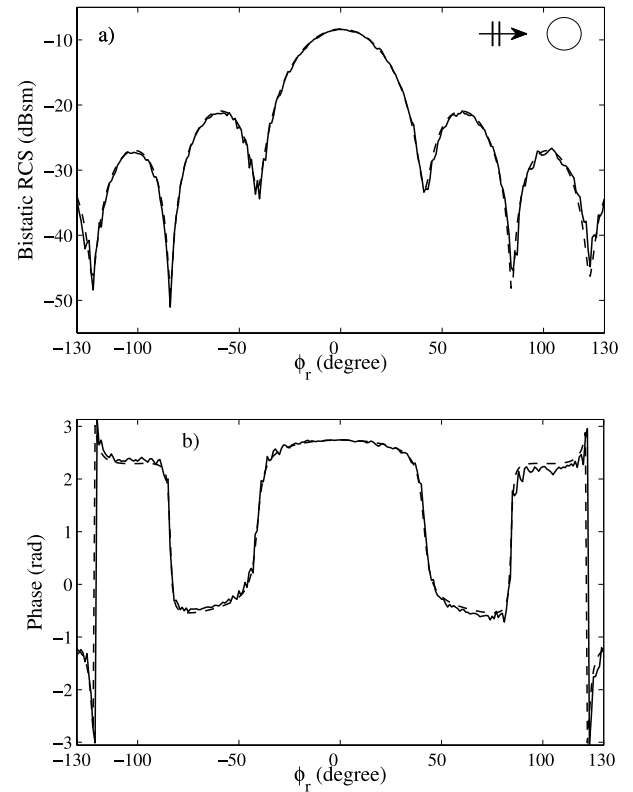


**Figure 5.** Comparison of (a)  $|E_{d,\theta\theta}|$  and (b)  $\arg(E_{d,\theta\theta})$ , measured (full line) and simulated (dashed line). This result is obtained for the Altuglass sphere at 8 GHz and for  $\phi_s = 90^\circ$  ( $\mathcal{F}_{\theta\theta} = 0.002$ ).

**Table 2.** Values of the Error Function  $\overline{\mathcal{F}_{\theta\bullet}}$  for the Altuglass Sphere as a Function of Frequency, Incidence Angle, and Polarization<sup>a</sup>

Frequency (GHz)	$\overline{\mathcal{F}_{\theta\theta}} \phi_s = 90^\circ$	$\overline{\mathcal{F}_{\theta\theta}} \phi_s = 60^\circ$	$\overline{\mathcal{F}_{\theta\phi}} \phi_s = 60^\circ$	$\overline{\mathcal{F}_{\theta\theta}} \phi_s = 30^\circ$	$\overline{\mathcal{F}_{\theta\phi}} \phi_s = 30^\circ$
2	0.019	0.238	0.450	0.193	0.260
3	0.023	0.065	0.128	0.137	0.095
4	0.003	0.027	0.064	0.045	0.043
5	0.002	0.009	0.060	0.052	0.033
6	0.003	0.011	0.074	0.054	0.028
7	0.003	0.014	0.196	0.043	0.109
8	0.002	0.014	0.032	0.030	0.035
9	0.005	0.023	0.047	0.034	0.054
10	0.009	0.025	0.121	0.038	0.107
11	0.007	0.020	0.134	0.064	0.099
12	0.011	0.038	0.067	0.070	0.112
13	0.014	0.037	0.069	0.047	0.070
14	0.012	0.049	0.121	0.095	0.110
15	0.010	0.092	0.060	0.071	0.079
16	0.006	0.049	0.078	0.058	0.107
17	0.015	0.097	0.271	0.090	0.097
18	0.011	0.145	0.265	0.103	0.157
$\overline{\mathcal{F}_{\theta\bullet}}$	0.009	0.056	0.127	0.072	0.094

<sup>a</sup>The mean value  $\overline{\mathcal{F}_{\theta\bullet}}$  on all the frequencies is given at the end of the table.

various source positions as well as for various polarization cases. This proves the accuracy of our measurement system.

#### 4. Modeling Codes

[23] In order to validate our measurements, we have simulated the response of the targets to a known excitation thanks to modeling codes. The scattering of an electromagnetic wave by an arbitrary three-dimensional scatterer is a complex problem. Many methods have been developed [Kahnert, 2003]. The first method that we are using is based on the well-known Mie theory [Born and Wolf, 1975] and has been used for the spherical obstacles.

[24] For the cubical obstacles or even more complex obstacles, in particular for those which are more depolarizing, we used the coupled dipole method (CDM) introduced by Purcell and Pennypacker to study the scattering of light by interstellar objects of arbitrary shape [Purcell and Pennypacker, 1973]. To give an idea of the computational burden, for a cubic object of side  $a = 80$  mm, 512 000 discretization cells were necessary. More information on the CDM can be found in the study of Chaumet *et al.* [2004].

[25] For both Mie and CDM methods, the incident field is taken as a plane wave of unit amplitude and phase origin at the middle of the target.

#### 5. Comparison Between Measured and Simulated Fields

##### 5.1. Targets Characteristics

[26] Field amplitude and phase measurements have been performed on a large frequency band and for four different

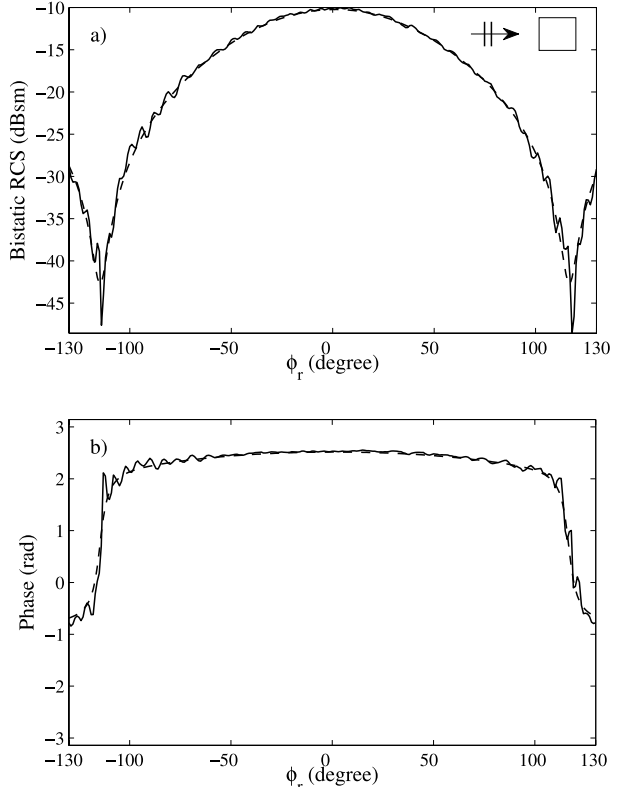


**Figure 6.** Comparison of (a)  $|E_{d,\theta\theta}|$  and (b)  $\arg(E_{d,\theta\theta})$ , measured (full line) and simulated (dashed line). This result is obtained for the Polyethylene cube at 2 GHz and for  $\phi_s = 90^\circ$  and  $\phi_o = 0^\circ$  ( $\mathcal{F}_{\theta\theta} = 0.001$ ).

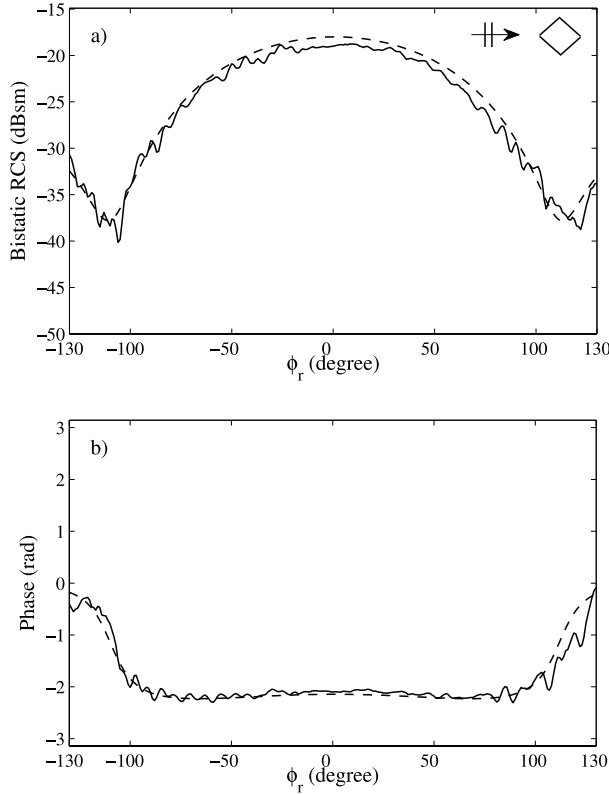


**Figure 7.** Comparison of (a)  $|E_{d,\theta\theta}|$  and (b)  $\arg(E_{d,\theta\theta})$ , measured (full line) and simulated (dashed line). This result is obtained for the Polyethylene cube at 2 GHz and for  $\phi_s = 30^\circ$  and  $\phi_o = -45^\circ$  ( $\mathcal{F}_{\theta\theta} = 0.013$ ).

targets, being either metallic or dielectric, symmetrical or not. The sizes of the targets are given in Table 1. In the computations, the metallic targets are considered to be perfectly conducting. This assumption is valid as the metallic objects are made of stainless steel and studied in the frequency range [2–18] GHz. For the dielectric targets, the permittivity  $\varepsilon_r$  was determined on a sample made of the same material as the target, thanks to measurements in a guided wave configuration (commercial kit EPSIMU; *Sabouroux and Boschi* [2005]) which permits to determine the relative permittivities with 5% to 10% accuracy (depending on the losses of the material). The obtained permittivities are presented in Table 1. They were found to be almost constant in the chosen frequency band and purely real.

## 5.2. Comparison Criterion

[27] In order to quantify the accuracy of the measurements, the experimental fields are compared to simulated ones. For each target, the comparison is made on the amplitude and on the phase of the diffracted field, thanks

to an error function defined for a given  $\phi_s$ , for a given  $\phi_o$  and for each frequency  $f$  by

$$\mathcal{F}_{\theta\bullet}(f) = \frac{\sum_{\phi_r} |E_{d,\theta\bullet}^{\text{simu}} - E_{d,\theta\bullet}^{\text{meas}}|^2}{\sum_{\phi_r} |E_{d,\theta\bullet}^{\text{simu}}|^2} \quad (2)$$

where  $\bullet$  stands for either  $\theta$  or  $\varphi$  according to the chosen polarization, and where  $E_{d,\theta\bullet}^{\text{simu}}$  (respectively  $E_{d,\theta\bullet}^{\text{meas}}$ ) corresponds to the simulated (respectively measured) scattered field. We also define by  $\overline{\mathcal{F}}_{\theta\bullet}$  the mean of  $\mathcal{F}_{\theta\bullet}$  on all the target orientations  $\phi_o$ , and by  $\overline{\mathcal{F}}_{\theta\bullet}$  the mean of  $\mathcal{F}_{\theta\bullet}$  on all the frequencies.

[28] All the measured fields have been treated first for systematic errors and then for drift errors [*Eyraud et al.*, 2006; *Eyraud*, 2006]. The complex calibration coefficient  $D$  is computed using equation (1) for each target.

## 5.3. Spherical Objects

[29] Figures 2, 3, and 4 show the results obtained for the metallic sphere for two different angles of incidence ( $\phi_s = 90$  and  $30^\circ$ ) and two frequencies (8 and 18 GHz). The fields are plotted in the standard Radar Cross Section

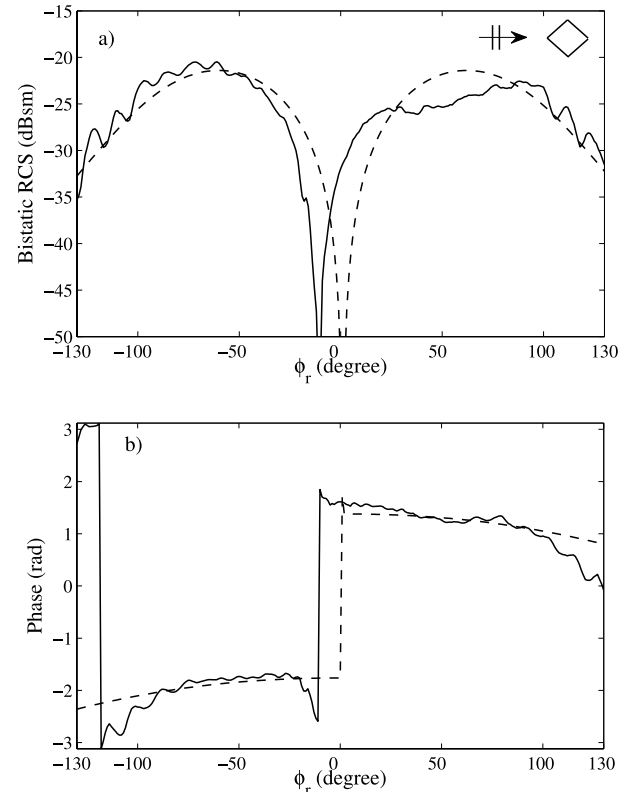


**Figure 8.** Same configuration as in Figure 7 but for  $|E_{d,\theta\varphi}|$  and  $\arg(E_{d,\theta\varphi})$  ( $\mathcal{F}_{\theta\varphi} = 0.074$ ).

**Table 3.** Values of the Error Function  $\mathcal{F}_{\theta\bullet}$  for the Polyethylene Cube at 8 GHz as a Function of Target Orientation, Incidence Angle, and Polarization<sup>a</sup>

$\phi_o$	$\mathcal{F}_{\theta\theta} \phi_s = 90^\circ$	$\mathcal{F}_{\theta\theta} \phi_s = 60^\circ$	$\mathcal{F}_{\theta\varphi} \phi_s = 60^\circ$	$\mathcal{F}_{\theta\theta} \phi_s = 30^\circ$	$\mathcal{F}_{\theta\varphi} \phi_s = 30^\circ$
-45°	0.018	0.116	0.312	0.092	0.065
0°	0.017	0.079	0.208	0.093	0.053
45°	0.014	0.108	0.280	0.100	0.047
90°	0.037	0.081	0.197	0.089	0.041
135°	0.014	0.133	0.296	0.073	0.032
$\overline{\mathcal{F}_{\theta\bullet}}$	0.020	0.103	0.259	0.089	0.048

<sup>a</sup>The mean value  $\overline{\mathcal{F}_{\theta\bullet}}$  on all the target orientations is given at the end of the table.

(RCS) form [Crispin and Siegel, 1968; Sarabandi *et al.*, 1990]. It can be noticed that we use a bistatic form of the RCS as the fields depend on  $\phi_r$ . From Figure 2a, one can see the quality of the symmetry of the scattered field. A good agreement is found between the measured data and the theoretical results even for a working frequency of 18 GHz. Theoretically, for  $\phi_s = 90^\circ$ ,  $|E_{d,\varphi}|$  should be equal to 0 for all values of  $\phi_r$ . From Figure 2a, one can see that  $|E_{d,\varphi}|$  is very small compared to  $|E_{d,\theta}|$ , but not equal to 0 (around 20 dB lower). The small bump in the middle of the curve is probably due to an imperfect linear antenna polarization state: the non ideal  $e_\varphi$  polarization of the incident field as well as the undesired sensitivity of the receiver to the  $e_\theta$  polarization. Anyway the amplitude of the remaining signal elsewhere is below the noise level of the measurements. From Figure 2b, one can see that even with rather fast phase variations with respect to  $\phi_r$ , the measured scattered field is still very close to the simulated one. From Figure 4, one can see the geometrical depolarization which leads to a non negligible amplitude  $|E_{d,\varphi}|$ . The agreement between experiment and theory is still very good and is significant of a good positioning accuracy of the target in the  $xOy$  plane.

[30] Figure 5 shows the results obtained for the Altuglass sphere with  $\phi_s = 90^\circ$  and a frequency of 8 GHz. One difficulty for dielectric scatterers is to get a precise determination of their relative permittivity. A permittivity value has first been measured with the EpsiMu commercial kit, providing  $\varepsilon_r = 2.50 \pm 0.13$ . This value has been refined by minimizing the error function of equation (2) to obtain a value of  $\varepsilon_r^{\text{opt}} = 2.60$ . This optimized value has been used for all the simulations. The values of the error function calculated for different values of  $\phi_s$  and different frequencies are represented in Table 2. For the lower part of the frequency range as the target is very small compared to the wavelength, the error functions  $\overline{\mathcal{F}_{\theta\bullet}}$  increase. At high frequencies, measurements are much more sensitive to positioning errors and here again the error functions  $\overline{\mathcal{F}_{\theta\bullet}}$  increase. Because of the smaller value of  $|E_{d,\theta\varphi}|$ , the value of  $\overline{\mathcal{F}_{\theta\varphi}}$  in this case is larger than  $\overline{\mathcal{F}_{\theta\theta}}$ . Nevertheless, the very low level of discrepancy is visible for all frequencies and incidence angles.

#### 5.4. Dielectric Cube

[31] Measurements on a Polyethylene cube have also been made. A permittivity value of  $\varepsilon_r = 2.30 \pm 0.12$  has been determined from the measurements in our coaxial cell. In terms of error functions, the best agreement between experiment and theory is obtained when  $\varepsilon_r^{\text{opt}} = 2.35$ . Figure 6 shows the results obtained at 2 GHz, which is our lower working frequency, with  $\phi_s = 90^\circ$  and

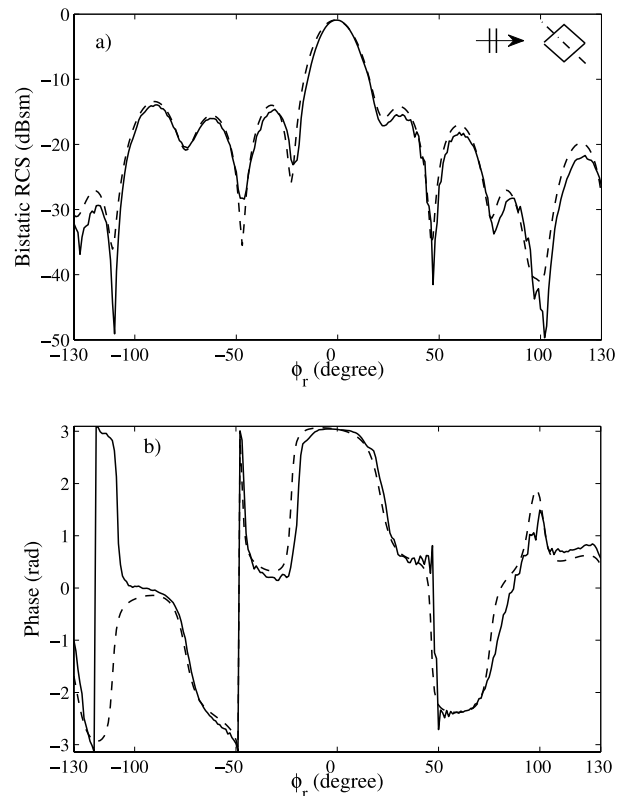


**Figure 9.** Comparison of (a)  $|E_{d,\theta\theta}|$  and (b)  $\arg(E_{d,\theta\theta})$ , measured (full line) and simulated (dashed line). This result is obtained for the Ertalon cylinder at 8 GHz and for  $\phi_s = 90^\circ$  and  $\phi_o = 45^\circ$  ( $\overline{\mathcal{F}_{\theta\theta}} = 0.026$ ).

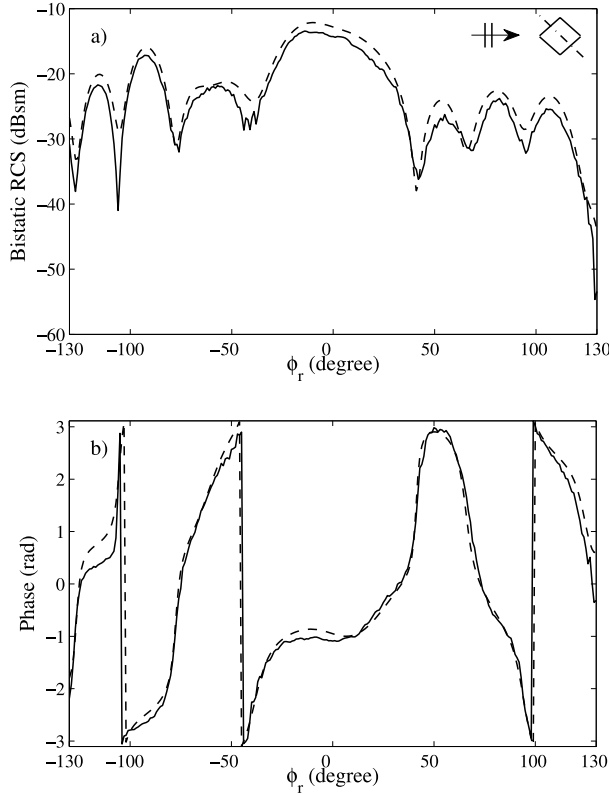


**Figure 10.** Comparison of (a)  $|E_{d,\theta\theta}|$  and (b)  $\arg(E_{d,\theta\theta})$ , measured (full line) and simulated (dashed line). This result is obtained for the Ertalon cylinder at 8 GHz and for  $\phi_s = 60^\circ$  and  $\phi_o = 45^\circ$  ( $\mathcal{F}_{\theta\theta} = 0.047$ ).

$\phi_o = 0^\circ$ . From Figure 6, one can see that the phase variations are limited because of the small ratio wavelength/size of the object for such a frequency (about half of a wavelength). The results obtained in the cross-polarization case, not represented here, show that there is still a residual signal whose amplitude is comparable to the one obtained with the spherical objects considered previously.

[32] The results represented in Figure 7 (for  $E_{d,\theta\theta}$ ) and Figure 8 (for  $E_{d,\theta\varphi}$ ) are obtained for the same cube, still at 2 GHz but with  $\phi_s = 30^\circ$  and  $\phi_o = -45^\circ$ . Here again, as in Figure 3, one can see the effect of the geometrical depolarization when the source moves outside the azimuthal plane. In this case, the levels of  $|E_{d,\theta\theta}|$  and  $|E_{d,\theta\varphi}|$  are comparable and the error functions are even a bit lower for this cross-polarization case. To understand the shift of the scattered field minimum observed in Figure 8, it should be first mentioned that in the cross-polarization case, misalignment is much more critical than in the copolarization case. As this shift is varying with the frequency, we can think that it is mainly due to

the imperfect polarizations of our antennas. In addition, the main lobe of the antenna pattern presents angular variations with the frequency, which adds to the perturbations. Moreover, the levels of the fields measured in front of the source are so small that the fields are very close to the noise floor. Finally, having a closer look to our error function, which compares the real part and the imaginary part of the fields, it leads to the conclusion that high scattered fields do have a stronger influence on its computation than small ones. Also, the phase differences which are visible in Figure 8 are not reflected in the error function because of its relative insensibility to the small values of the fields. To give an idea of the agreement between simulated and measured fields for different object orientations, the error functions variations at 8 GHz are summarized in Table 3.

### 5.5. Dielectric Cylinder

[33] The last target is an Ertalon cylinder. Measurements in the coaxial guide configuration have given a permittivity value,  $\varepsilon_r = 3.00 \pm 0.15$ . The minimum value of the error function was reached when  $\varepsilon_r^{opt} = 3.05$ . The results obtained at 8 GHz with  $\phi_s = 90^\circ$  and  $\phi_o = 45^\circ$

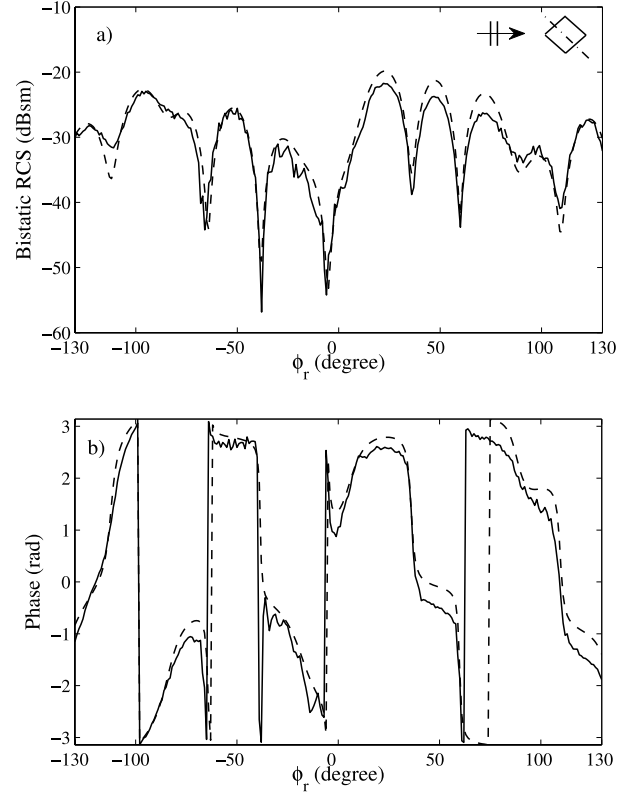


**Figure 11.** Same configuration as in Figure 10 but for  $|E_{d,\theta\varphi}|$  and  $\arg(E_{d,\theta\varphi})$  ( $\mathcal{F}_{\theta\varphi} = 0.118$ ).

**Table 4.** Values of the Error Function  $\mathcal{F}_{\theta\bullet}$  for the Ertalon Cylinder at 8 GHz as a Function of Target Orientation, Incidence Angle, and Polarization<sup>a</sup>

$\phi_o$	$\mathcal{F}_{\theta\theta} \phi_s = 90^\circ$	$\mathcal{F}_{\theta\theta} \phi_s = 60^\circ$	$\mathcal{F}_{\theta\varphi} \phi_s = 60^\circ$	$\mathcal{F}_{\theta\theta} \phi_s = 30^\circ$	$\mathcal{F}_{\theta\varphi} \phi_s = 30^\circ$
-45°	0.004	0.055	0.119	0.058	0.065
0°	0.033	0.085	0.144	0.094	0.155
45°	0.026	0.047	0.118	0.088	0.115
90°	0.014	0.041	0.081	0.095	0.139
$\mathcal{F}_{\theta\bullet}$	0.019	0.057	0.116	0.084	0.119

<sup>a</sup>The mean value  $\mathcal{F}_{\theta\bullet}$  on all the target orientations is given at the end of the table.

(respectively  $\phi_s = 60^\circ$  and  $\phi_o = 45^\circ$ ) are represented in Figure 9 (respectively Figure 10 and Figure 11). In this case, as expected, no symmetry is observed on the curves and this allows to be rather confident on both measurements and the CDM computations. The discrepancy observed between the phases of the measured and simulated fields in Figure 9b for  $\phi_r$  below  $-75^\circ$  can be explained by the very small level of both the real part and the imaginary part of the scattered fields for such scattering angles (see the magnitude plot). This leads therefore to a very unstable determination of the phase. The other major difference between the measured and simulated fields observed in Figure 11 is mainly due to phase wrapping. However, as phase unwrapping representation drastically reduces the dynamics of the curves, we prefer to avoid it. To give an idea of the agreement between simulated and measured fields, the error functions variations at 8 GHz are summarized in Table 4.

## 6. Measurement Accuracy

[34] To highlight the good accuracy of our measurement system, two aspects have been analyzed. The first one concerns the positioning of the target, which must be precisely placed inside a 4 m diameter measurement sphere. The second one is a consequence of the measurement accuracy and concerns the permittivity value of the obstacles.

### 6.1. Target Positioning Along the $z$ Axis

[35] The center of the target is aligned with the rotation axis of the object-motor thanks to a laser diode which is used as a pointer. To align the global setup, the laser diode is alternatively fixed at the receiving and at the transmitting antenna locations. In previous works [Eyraud, 2006], we have been able to determine that the target position accuracy is of the order of  $\pm 0.1$  mm in the  $x$  and  $y$  directions. As we are now measuring outside of the azimuthal plane, we can also gain some insights on the vertical positioning accuracy.

[36] To check the positioning accuracy along the  $z$  axis, we have measured the scattered field along the arch by varying the transmitting antenna position  $\phi_s$ , keeping the target position fixed and the receiver position at  $\phi_r = 0^\circ$ . The measured target is the Altuglass sphere. In Figure 12, the phase of the scattered field measured for  $\phi_s$  varying between  $0^\circ$  and  $160^\circ$  is plotted for several  $z$ -positions of the target in order to assess the sensitivity to the target altitude.

[37] The accuracy along the  $z$  axis has been estimated to be  $\pm 0.3$  mm. The positioning is more accurate in the  $xOy$  plane than in the vertical one, because of the alignment protocol: in the horizontal plane, the target is rotated several times around the  $z$  axis, but we cannot rotate it around the  $y$  axis in the  $xOz$  plane.

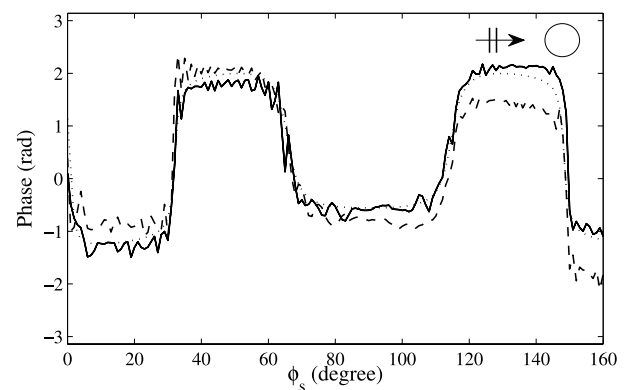


**Figure 12.**  $\arg(E_{d,\theta\theta})$  for a source moving on the arch. This result is obtained for the Altuglass sphere at 11 GHz and for  $\phi_o = \phi_r = 0^\circ$ . Dashed line: measured with a target presumably positioned at  $O$  ( $\mathcal{F}_{\theta\theta} = 0.100$ ). Full line: measured with a target positioned 2.3 mm below the previous position ( $\mathcal{F}_{\theta\theta} = 0.047$ ). Dotted line: simulated with the target centered at  $z = 0.0$  mm.

**Table 5.** Values of the Error Function  $\mathcal{F}_{\theta\theta}$  for Various Permittivities Values and for Different Materials, Obtained at 8 GHz and for  $\phi_s = 90^\circ$

	$\mathcal{F}_{\theta\theta} \varepsilon_r = \varepsilon_r^{opt} - 0.05$	$\mathcal{F}_{\theta\theta} \varepsilon_r = \varepsilon_r^{opt}$	$\mathcal{F}_{\theta\theta} \varepsilon_r = \varepsilon_r^{opt} + 0.05$
Altuglass	0.006	0.002	0.005
Polyethylene	0.047	0.021	0.029
Ertalon	0.031	0.018	0.024

## 6.2. Permittivity Optimization

[38] The results obtained so far may also suggest a free space scattering method for an accurate determination of the global relative permittivity for various targets (a precision of about 1% being achievable). Indeed, as it can be seen in Table 5, permittivity variations have visible effects on the error function. The optimized relative permittivities, obtained with Ertalon, Polyethylene and Altuglass, are in full agreement (see Table 1) with values found in the literature such as the National Institute of Standards and Technology (NIST) cavity measurements [Riddle *et al.*, 2003]. Therefore the non invasive relative permittivities measurements may be of particular interest when the global permittivity of an homogeneous manufactured object of known shape has to be determined (e.g., radoms, dielectric lenses, . . .). This is just the first step toward a complete determination of the shape and electromagnetic characteristics of unknown homogeneous or inhomogeneous objects from their scattered fields.

## 7. Conclusion

[39] Since the 2D database measurements presented by Belkebir and Saillard [2001, 2005]; Geffrin *et al.* [2005], strong efforts have been made to improve our measurement setup and to extend its domain of application to the 3D case. In this paper, we present the results obtained with our 3D setup. The very good agreement between experimental and numerical results obtained for dielectric and metallic targets, in copolarization and cross-polarization cases, demonstrates the correct behavior of our system.

[40] 3D measurements can have direct applications for analyzing scattering from targets with complex shapes, made of different materials with various intrinsic properties, e.g., inhomogeneous, dispersive or with magnetic properties, or for studying, thanks to a scale translation, the light scattering of particles aggregates [Sabouroux *et al.*, 2007].

[41] This study is also a prerequisite step toward inverse 3D scattering applications, where people are interested in determining the dielectric characteristics of unknown scatterers from their electromagnetic signature. The results presented therein make us confident in

the realization of a new 3D database as a continuation of the ones presented in [McGahan and Kleinman, 1996, 1997, 1999a, 1999b; Belkebir and Saillard, 2001, 2005]. We are also confident in providing this new 3D database as we are able to provide error bars associated with each measurement points [Eyraud, 2006].

[42] We have also shown that we can use our system to recover information on the permittivity value of the scatterer with an accuracy of around 1% for lossless dielectric materials. This can be a good option for measuring in a non-destructive way the average permittivity of a material, using for example a reduced-order model [Budko and Remis, 2004].

[43] **Acknowledgments.** The authors thank for their precious help G. Geurt, R. Hugounenc, J.-P. Spinelli, P. Lewilly, and B. Stout.

## References

- Belkebir, K., and M. Saillard (2001), Special section on testing inversion algorithms against experimental data, *Inverse Problems*, **17**, 1565–1571.
- Belkebir, K., and M. Saillard (2005), Special section on testing inversion algorithms against experimental data: Inhomogeneous targets, *Inverse Problems*, **21**, S1–S4.
- Borden, B. (2002), Topical review: Mathematical problems in radar inverse scattering, *Inverse Problems*, **18**, R1–R28.
- Born, M., and E. Wolf (1975), *Principles of Optics*, Pergamon Press, Oxford, U. K.
- Bradley, J., P. J. Collins, J. Fortuny-Guash, M. L. Hastriter, G. Nesti, A. J. Terzuoli, and K. S. Wilson (2005), An investigation of bistatic calibration techniques, *IEEE Trans. Geosci. Remote Sens.*, **43**, 2185–2191.
- Budko, N. V., and R. F. Remis (2004), Electromagnetic inversion using a reduced-order three-dimensional homogeneous model, *Inverse Problems*, **20**, S17–S26.
- Chaumet, P. C., A. Sentenac, and A. Rahmani (2004), Coupled dipole method for scatterers with large permittivity, *Phys. Rev. E*, **70**, 036,606-6.
- Coté, M. G. (1992), Automated swept-angle bistatic scattering measurements using continuous wave radar, *IEEE Trans. Instrum. Meas.*, **41**, 185–192.
- Crispin, J., and K. Siegel (1968), *Methods of Radar Cross-section Analysis*, Academic Press, New York.
- Eyraud, C. (2006), Caractérisation et optimisation, dans le domaine des hyperfréquences, des mesures de champs dif-

- fractés. Applications aux problèmes directs et inverses tridimensionnels, Ph.D. thesis, Univ. of Provence, Marseille, France.
- Eyraud, C., J.-M. Geffrin, A. Litman, P. Sabouroux, and H. Giovannini (2006), Drift correction for scattering measurements, *Appl. Phys. Lett.*, **89**, 244,104.
- Fortuny-Guasch, J. (2002), A novel 3d subsurface radar imaging technique, *IEEE Trans. Geosci. Remote Sens.*, **40**, 443–452.
- Geffrin, J.-M., P. Sabouroux, and C. Eyraud (2005), Free space experimental scattering database continuation: Experimental setup and measurement precision, *Inverse Problems*, **21**, S117–S130.
- Gurel, L., H. Bagci, J. C. Castelli, A. Cheraly, and F. Tardivel (2003), Validation through comparison: Measurement and calculation of the bistatic radar cross section (BRCS) of a stealth target, *Radio Sci.*, **38**(3), 1046, doi:10.1029/2001RS002583.
- Gustafson, B. A. S. (1996), Microwave analog to light scattering measurements: A modern implementation of a proven method to achieve precise control, *J. Quant. Spectrosc. Radiat. Transfer*, **55**, 663–672.
- Hauck, B., F. Ulaby, and R. DeRoo (1998), Polarimetric bistatic measurement facility for point and distributed targets, *IEEE Trans. Antennas Propag.*, **40**, 31–40.
- HP Antenna Guide (1990), *Agilent 85301B/C antenna measurement systems 45 MHz to 110 GHz, configuration guide*, no 5967-6042E. (Available at <http://cp.literature.agilent.com/litweb/pdf/5967-6042E.pdf>)
- Kahnert, F. M. (2003), Numerical methods in electromagnetic scattering theory, *J. Quant. Spectrosc. Radiat. Transfer*, **79–80**, 775–824.
- Kahny, D., K. Schmitt, and W. Wiesbeck (1992), Calibration of bistatic polarimetric radar systems, *IEEE Trans. Geosci. Remote Sens.*, **30**, 847–852.
- McGahan, R. V., and R. E. Kleinman (1996), Special session on image reconstruction using real data, *IEEE Antennas Propag. Mag.*, **38**, 39–59.
- McGahan, R. V., and R. E. Kleinman (1997), Second annual special session on image reconstruction using real data, *IEEE Antennas Propag. Mag.*, **39**, 7–32.
- McGahan, R. V., and R. E. Kleinman (1999a), Third annual special session on image reconstruction using real data: part 1, *IEEE Antennas Propag. Mag.*, **41**, 34–51.
- McGahan, R. V., and R. E. Kleinman (1999b), Third annual special session on image reconstruction using real data: part 2, *IEEE Antennas Propag. Mag.*, **41**, 20–40.
- Purcell, E. M., and C. R. Pennypacker (1973), Scattering and absorption of light by nonspherical dielectric grains, *Astrophys. J.*, **186**, 705–714.
- Riddle, B., J. Baker-Jarvis, and J. Krupka (2003), Complex permittivity measurements of common plastics over variable temperatures, *IEEE Trans. Microwave Theory Tech.*, **51**, 727–733.
- Sabouroux, P., and P. Boschi (2005), EpsiMu: A new microwave materials measurements kit, *Rev. Electr. Electr.*, **10**, 58–62.
- Sabouroux, P., J.-M. Geffrin, and C. Eyraud (2005), An original microwave near-field/far-field spherical setup: Applications to antennas and scattered field measurements, in *Proc. of Antenna Measurement Techniques Assoc. Symposium*, edited by Société de l'Electricité, de l'Électronique et des Technologies de l'Information et de la Communication (SEE), pp. 292–296, Paris, France.
- Sabouroux, P., B. Stout, J.-M. Geffrin, C. Eyraud, I. Ayrancı, N. Selcuk, and R. Vaillon (2007), Amplitude and phase of light scattered by micro-scale aggregates of dielectric spheres: Comparison between theory and microwave analogy experiments, *J. Quant. Spectrosc. Radiat. Transfer*, **103**, 156–167.
- Sarabandi, K., F. Ulaby, and M. Tassoudji (1990), Calibration of polarimetric radar systems with good polarization isolation, *IEEE Trans. Geosci. Remote Sens.*, **28**, 70–75.
- van den Berg, P. M., M. G. Coté, and R. E. Kleinman (1995), Blind shape reconstruction from experimental data, *IEEE Trans. Antennas Propag.*, **43**, 1389–1396.
- Whitt, M., F. Ulaby, P. Polatin, and V. Liepa (1991), A general polarimetric radar calibration technique, *IEEE Trans. Antennas Propag.*, **39**, 62–67.

---

P. C. Chaumet, J.-M. Geffrin, H. Giovannini, A. Litman, P. Sabouroux, and H. Tortel, Institut Fresnel, Aix-Marseille Université, CNRS, Ecole Centrale Marseille, Domaine Universitaire de Saint-Jérôme, Case 162, 13397 Marseille Cedex, France. (jean-michel.geffrin@fresnel.fr)

C. Eyraud, Laboratoire de Planétologie de Grenoble, BP 53, 38041 Grenoble Cedex, France.